Theor Chem Acc (2012) 131:1091
DOI 10.1007/s00214-012-1091-4

REGULAR ARTICLE

The bonding in hexagonal $Ba_{2/3}Pt_3B_2$ and $CeCo_3B_2$ type ternary metal borides

Seeyearl Seong · Sik Young Choi · Thomas A. Albright

Received: 31 March 2011 / Accepted: 25 May 2011 / Published online: 11 February 2012

Abstract Tight-binding calculations with an extended Hückel Hamiltonian were performed on $Ba_{2/3}Pt_3B_2$ and $LuOs_3B_2$. Hypothetical linear metal boride chains present in these materials are analyzed with a three-dimensional model that contains a trigonal bipyramidal T_3B_2 (T = transition metal) building unit for the compounds. The geometrical structure for the T_3B_2 trigonal bipyramids depends on the number of electrons. For systems that have greater than 36 electrons in its trigonal bipyramidal building unit, a structural distortion is expected. Electron back donation from the electron-rich M_3 fragment to the empty e′ set on B_2 creates boron–boron interaction along the *z*-axis. Boron–boron pairing then participates as an electron sink and causes a trigonal distortion of the platinum Kagome net. On the other hand, a system with <35 electrons should have an undistorted, $CeCo_3B_2$ type structure. The electronic factors that create the breathing motion are discussed and analyzed with the aid of molecular and solid-state models. The metal–metal bonding associated with the structural properties also has been examined.

Keywords Tight-binding calculations · Transition metal borides · Band structure calculations · Kagome net

1 Introduction

Intermetallic bonding in inorganic compounds for many years has been a favorite subject of material science. The existence of intermetallic or metal–metal bonding leads to entirely new structures, particularly among the transition metal compounds. In these structures, metal–metal bonding manifests itself by the formation of clusters such as triangles, tetrahedra, octahedra, chains, and dimers within the lattice [1–4]. As the metal lattice breaks up into clusters, it is common that three-dimensional metal–metal bonding is still retained (to a lesser extent) with long inter-cluster distances, about 12–20% larger than in the bulk metal. A series of low T_c superconducting compounds with the composition MT_4B_4 (M = a rare earth element, T = a transition metal) form cubane-like clusters [5, 6]. The discovery of these compounds catalyzed intense research on potential ternary superconductor systems [7]. A related class of materials has been reported for the MCo_3B_2 system (M = Sc, Y, U or one of the rare earth elements) [8–13] that has the hexagonal $CeCo_3B_2$ type structure (P6/mmm). Here, the basic cluster building block is a T_3B_2 trigonal bipyramid. This structure is also found for ternary boride systems with general formulae: MRu_3B_2 (M = La, Ce, Pr, Nd, Sm, Gd, Tb, Dy, Ho, Er, Yb, Lu, Y, Th, or U), MOs_3B_2 (M = Lu or U), and MIr_3B_2(M = La, Th or U) [14]. Most members of these systems were reported to be either superconducting or magnetically ordered. For example,

Dedicated to Professor Eluvathingal Jemmis and published as part of the special collection of articles celebrating his 60th birthday; dedicated also in memoriam of Dr. Seeyearl Seong.

Seeyearl Seong: Deceased.

S. Seong · S. Y. Choi · T. A. Albright (✉)
Department of Chemistry, University of Houston,
Houston, TX 77204-5003, USA
e-mail: talbright@uh.edu

Present Address:
S. Y. Choi
Department of Applied Chemistry,
Andong National University, Andong 760-749, Korea

$LuOs_3B_2$ is a superconductor with a transition temperature of 4.6 K [14]. Structural variants of the hexagonal $CeCo_3B_2$ type have been reported, such as $ErIr_3B_2$ (C2/m) [15], $LaRu_3Si_2$ ($P6_3/m$) [16, 17], $ZrCo_3B_2$ (R3) [18], and URu_3B_2 (P3) [19], which have a large unitcell and lower symmetry. Defect structure types with compositions $M_{<1}T_3B_2$ have been observed. For example, $Ba_2Pt_9B_6$ (P63/mmc) [20], $Ba_2Ni_9B_6$ (R3) [21], and $La_{1-x}Rh_3B_2$ (P6/mmm) [15]. Specifically, $M_{2/3}Pt_3B_2$ (M = Ca, Sr or Ba) systems have superconducting transition temperatures from 1.7 to 5.7 K [20].

Most of the MT_3B_2 compounds have the $CeCo_3B_2$ type structure; a view in two perspectives is presented in Fig. 1. The M cations form a simple hexagonal lattice along with the B atoms and the T atoms form a Kagome(3636) net [22, 23].[1] Each T_3 triangle is capped with boron atoms below and above to give a trigonal bipyramid. These trigonal bipyramids are then joined in three dimensions by sharing vertices. The metal–metal distances in the $CeCo_3B_2$ type compounds are 2.50–2.75 Å, which are close to the values in the respective transition metals. For example, in $LuOs_3B_2$ [14], the Os–Os distances within the Kagome net are 2.73 Å, which is close to that in osmium metal; those distances between the osmium layers are more than 10% longer (3.05 Å). The B–B distances are 3.03 Å both within a Lu–B layer and between two such layers; therefore, the boron atoms are isolated from each other. The Lu atoms form chains along the c-axis (d[Lu–Lu] = 3.05 Å), and these chains are also isolated from each other (d[Lu–Lu] = 5.46 Å).

The $Ba_{2/3}Pt_3B_2$ structure [20] is derived from the $CeCo_3B_2$ type. In $Ba_{2/3}Pt_3B_2$, only two-thirds of the M positions are occupied by Ba. The Kagome net of Pt atoms undergoes a distortion as shown for the Pt atoms in **1**. The Pt–Pt distances are 2.86 Å within a small Pt

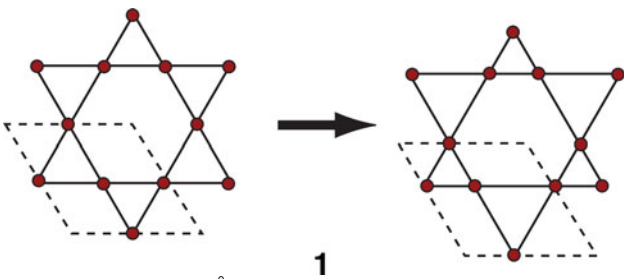

1

triangle and 3.30 Å between them. In contrast to the $CeCo_3B_2$ type, $Ba_{2/3}Pt_3B_2$ has an interlayer Pt–Pt distance of only 2.65 Å, as shown in Fig. 2a, which is 4.3% shorter than in Pt metal. One may find a similar distortion in Laves phases (the $MgZn_2$ type) [24–27] where every second triangle is capped by zinc atoms above and below the

[1] This nomenclature means that counting the rings around any vertex from one of the triangles we encounter, in order, a triangle is followed by a hexagon.

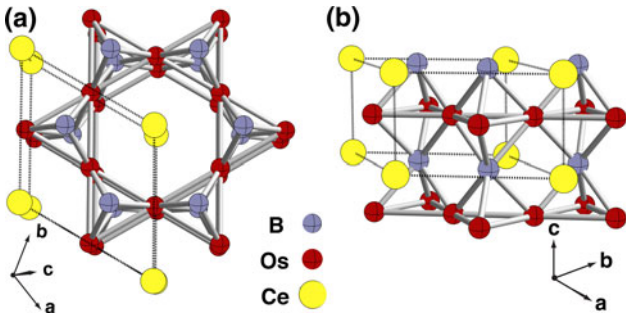

Fig. 1 A plot of the $CeCo_3B_2$ structure from the top (**a**), and side (**b**), view; the *dashed line* in each structure shows the unit cell

Kagome plane. Thus, the nature of the transition metal sublattice in $Ba_{2/3}Pt_3B_2$ is qualitatively different from that in $CeCo_3B_2$ in which two-dimensional clusters are formed. The Pt atoms in $Ba_{2/3}Pt_3B_2$ [20] can be viewed as forming zigzag chains (d[Pt–Pt] = 2.65 Å) running in the **c** direction, where the interchain distances are d[Pt–Pt] = 2.86 and 3.30 Å. In hexagonal MT_3B_2 phases of the $CeCo_3B_2$ type, the boron atoms form a hexagonal net; however, the layers are isolated from each other. In some distorted structures, e.g., $Ba_{2/3}Pt_3B_2$, they pair along the **c** direction [28–30]. In $Ba_{2/3}Pt_3B_2$, a one-dimensional deformation along **c**-axis of the boron chain provides short (2.29 Å) and long (2.98 Å) B–B distances. The short B–B distance is 33% longer than the usual B–B bond length of 1.70–1.74 Å. Nonetheless, this certainly represents sizable overlap between the boron atoms.

In present study, we shall investigate the electronic structure of $LuOs_3B_2$, which has the lowest number of valence electrons per formula unit (33 electrons) as a representative of the $CeCo_3B_2$ type of compound and $Ba_{2/3}Pt_3B_2$, which has the largest number of valence electrons per formula unit (37.33 electrons) as that for one distorted variant. Both structures are prevalent for a large number of alkali/lanthanide cation and transition metal combinations. Furthermore, there are a number of MT_3Si_2 analogs that also have the $CeCo_3B_2$ structure [31–33]. Previous calculations on compounds with the $CeCo_3B_2$ structure have focused on the magnetism and conductivity aspects [34–37]. Our concerns are perhaps more fundamental. We wish to understand the bonding in these compounds from an orbital point of view. Furthermore, we will investigate the electronic source of the distortion upon going from the $CeCo_3B_2$ structure to the $Ba_{2/3}Pt_3B_2$ one. All MT_3B_2 compounds are electron rich. The unifying geometrical feature in these materials is the presence of trigonal bipyramids. The application of Wade's rules and its variants [38–42] is problematic because of the unusual coordination around each transition metal. Nevertheless, consider in $Ba_{2/3}Pt_3B_2$ that the Pt–Pt distances of 2.65 and 2.86 Å correspond to single bonds, while those at 3.30 Å

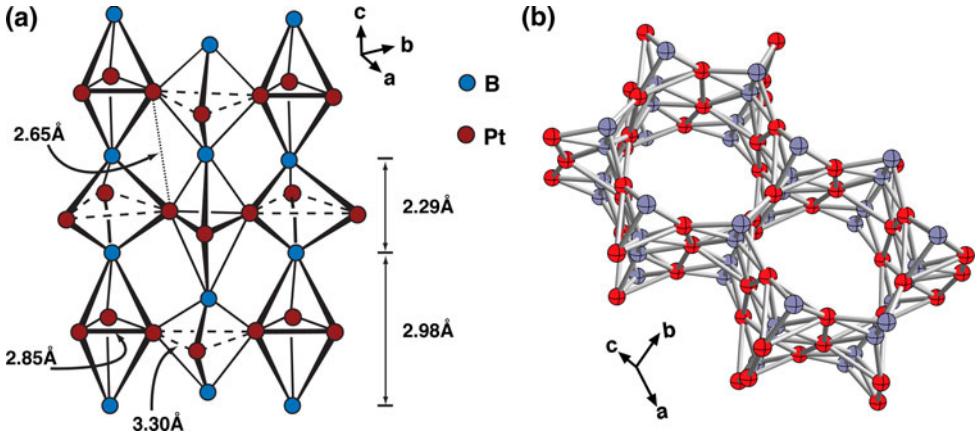

Fig. 2 Side (**a**), and top (**b**), views of the $Ba_{2/3}Pt_3B_2$ structure

do not constitute a bond. Furthermore, if the B–B distances at 2.29 Å are considered to be single bonds, then $Ba_{2/3}Pt_3B_2$ has a skeletal electron count of 17.33 electrons. Wade's rule dictates that 12 skeletal electrons should be stable for a trigonal bipyramidal cluster [43]. Even for $LuOs_3B_2$, a total of 13 skeletal electrons are present. The electronic factors shall be studied, which drive the distortion toward these two structural types, as well as, others having an intermediate number of valence electrons [18, 19, 44, 45]. Our operational strategy in the manuscript is to first consider a discrete trigonal bipyramid, followed by a one-dimensional model and then the full three-dimensional case for $Ba_{2/3}Pt_3B_2$. We employed a tight-binding [46] method within the extended Hückel [47–49][2] framework.

2 The T_3B_2 trigonal bipyramid

Triangular platinum clusters have been well studied both experimentally and theoretically [50–64]. An equilateral metal framework is expected for a 42 valence electron Pt_3 cluster molecule in which acceptor ligands bridge each platinum atom (e.g., $Pt_3(CNR)_6$). When two extra electrons are added, previous calculations have shown that distortion is favored to an isosceles triangle or to a larger equilateral triangle [50–65]. The molecular orbital diagram of a trigonal bipyramidal Pt_3B_2 unit is presented in Fig. 3. A $Pt_3B_2^{2-}$ unit is constructed by capping two boron atoms both above and below the Pt_3 triangle. We have arbitrarily partitioned the molecule into B_2^{2-} and neutral Pt_3 fragments. The $Pt_3B_2^{2-}$ molecular orbitals are fairly complicated since many of the Pt–Pt bonding and antibonding orbitals can mix with each other based on their symmetry properties. We may simply summarize the interaction as follows: Starting with the $2\sigma_g^+$ and $1\sigma_u^+$ B_2^{2-} combinations, the a_1' molecular orbital, **2**, is an

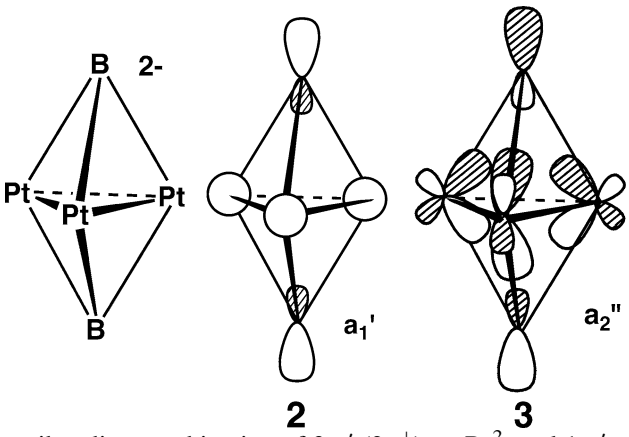

2 **3**

antibonding combination of $3a_1'$ ($2\sigma_g^+$) on B_2^{2-} and $1a_1'$ on the platinum fragment. There also is a second-order mixing of the Pt *sp* combination, $2a_1'$ which keeps the molecular a_1' orbital at moderate energies. The a_2'' molecular orbital at lower energy is the antibonding interaction of $2a_2''$ ($1\sigma_u^+$) on B_2^{2-} and $1a_2''$ of the platinum fragment. The highest occupied orbital is a degenerate e′ set. It consists of the bonding combination between the B_2^{2-} 3e′ ($1\pi_u$) set and the Pt_3 2e′ set. There are also second-order mixings of platinum $d_{x^2-y^2}$ and d_{z^2} orbital combinations that have e′ symmetry and the resultant molecular orbitals may be depicted as in **4** and **5**. It is

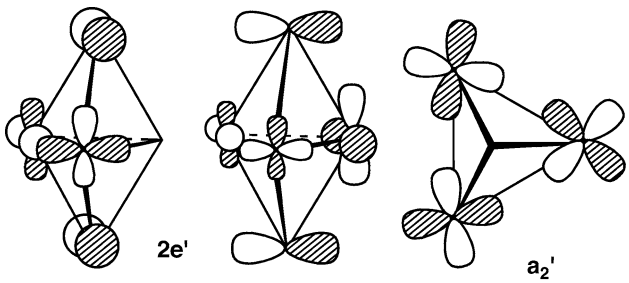

4 **5** **6**

important to realize that **4** and **5** have substantial Pt *s* character. In fact the overlap between the 3e′ fragment orbitals on B_2^{2-} and the 2e′ set on Pt_3, $\langle 3e'|2e'\rangle = 0.279$, whereas $\langle 3e'|1e'\rangle = 0.057$. Ultimately, the occupation of the Pt_3 2e′

[2] The parameters used were taken from [56, 65, 66].

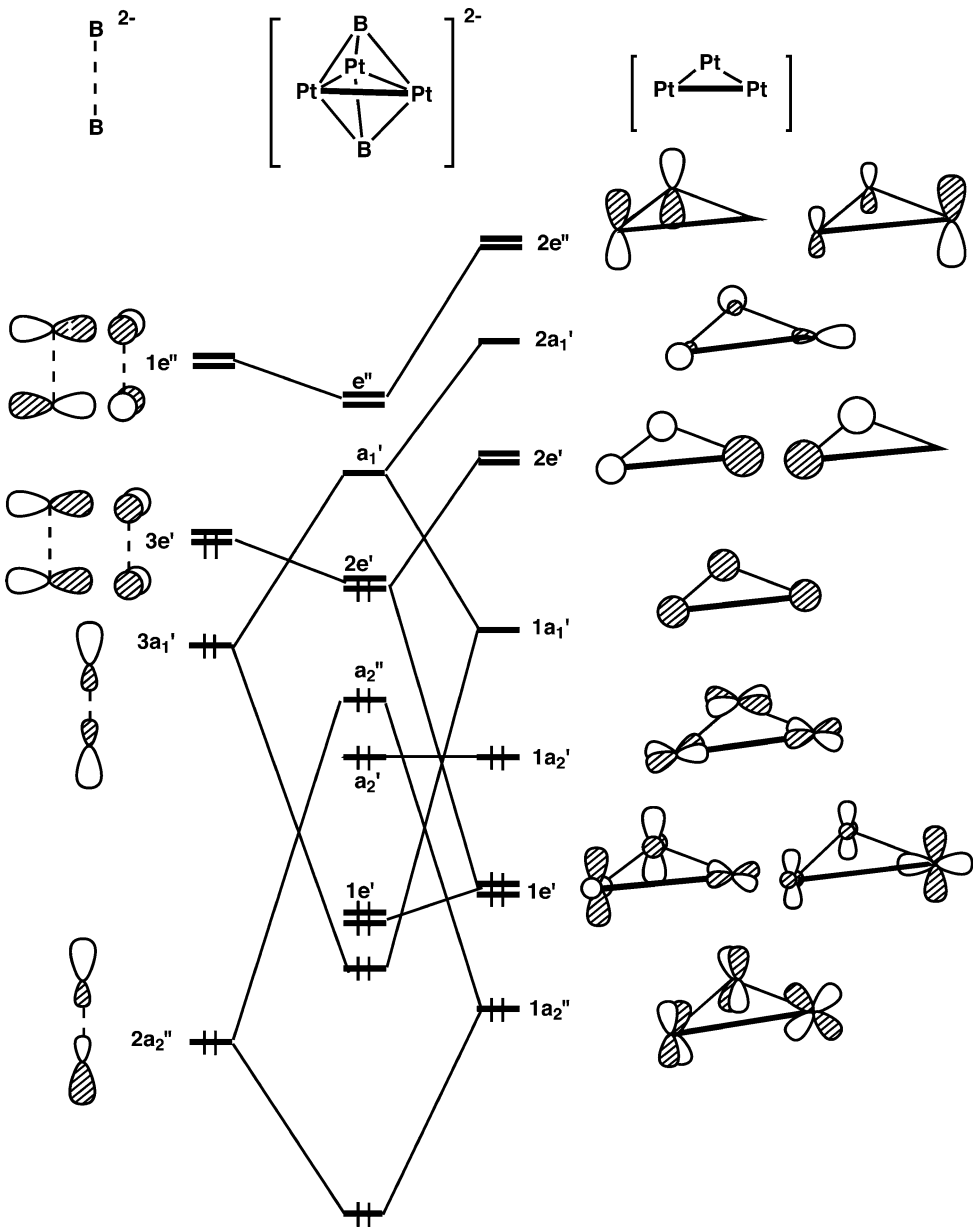

Fig. 3 The orbital interaction diagram for interacting a Pt_3 *triangle* with a capping B_2^{2-} unit

fragment orbitals was calculated to be 0.92 electrons. $3a_1'$ and $2a_2''$ on B_2^{2-} donate 0.82 and 0.36 electrons, respectively, to the Pt_3 fragment. The exact magnitude of these numbers is not important. The qualitative picture that emerges is that electron density is transferred from boron to platinum. We shall have more to say about this in the future. The molecular a_2' orbital, **6**, contains no boron character and is strongly Pt–Pt antibonding. Notice that occupation of the molecular 2e′, a_1' and a_2'' levels span the range of electron counts, from 38 to 36, that are of interest in the solid-state compounds. Notice that all of these MOs have large contributions of Pt *s* (and *p*) character. Finally, we shall also see remnants of a higher lying set of molecular orbitals, e″ as shown in **7** and **8**. Here Pt

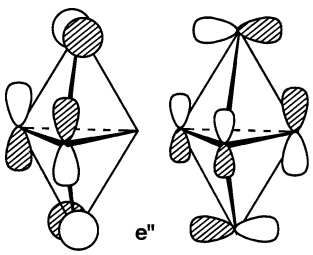

7 **8**

mixes with the 1e″ (π_g) set on B_2^{2-}. The B–B and Pt–Pt interactions described above determine the shape of a T_3B_2 trigonal bipyramidal unit, as well as, the three-dimensional structure of the solid state.

3 The one-dimensional Pt_3B_2 chain

To investigate the metal–metal and boron–boron interactions along the **c**-axis in the $Pt_3B_2^{-4/3}$ unit, we have performed band calculations for a one-dimensional B_2Pt_6 chain. Two different chains have been considered: the prototype structure, **9**, and the distorted type, as shown in **10**. A breathing motion for **9**, as shown, creates two different types of trigonal

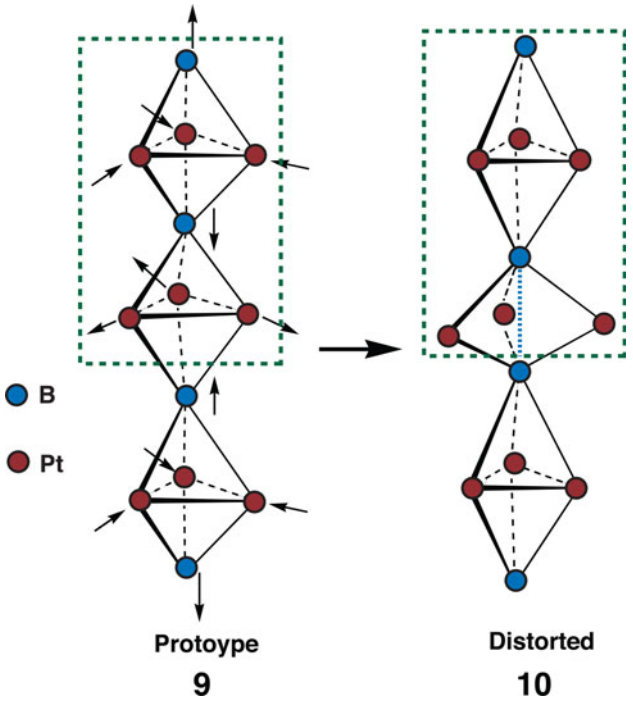

bipyramids, squashed, and elongated ones. Recall that there is substantial boron–boron interaction in the experimental structure, the elongated trigonal bipyramids (illustrated by the dotted blue line in **10**), but no Pt–Pt bonding within the trigonal bipyramid. However, the reverse is true for the squashed trigonal bipyramids. Here, it is important to note that the Pt–B distances were held constant during the breathing motion. Consequently, the Pt–Pt distance between trigonal bipyramids does increase on going from **9** to **10**. The unit cell for each structure is drawn within the green dashed rectangle for both structures. We will address this issue of interlayer metal–metal bonding later. A portion of the band structure for the prototype and distorted structure are shown in Fig. 4a and b, respectively. Arrows on the energy scale also indicate the position of the Fermi level for two electron counts. The wave vector runs from $k = 0$ (**Γ**) to $k = \pi/a$ (**A**). Starting with the prototype structure, the form of the wavefunction for the 2e′ and 2e″ bands is shown in **11**. At the **Γ** point, 2e″ is nothing more than the e″ set for the $B_2Pt_3^{2-}$ molecule shown in **7** and **8**. The 2e′ set is akin to molecular 2e′ (**4** and **5**) except that it is primarily Pt *s* and B *p* in character. The 2e″ band is stabilized on going to **A**, whereas the 2e′ band is destabilized. If a BPt_3 unit cell were chosen, 2e″ and 2e′ are

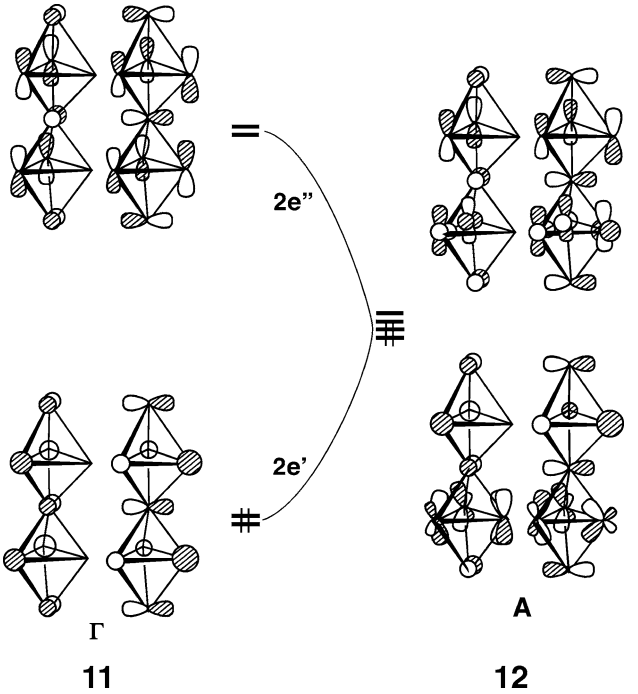

combined to give one e set which starts at **Γ** being primarily Pt *s* and ends at **A** with Pt *p*. In other words, this band is simply folded back when the unit cell is doubled. The same folding back occurs in the 1e′/1e″ set. These bands are primarily Pt *d* in character and correspond to the molecular 1e′ set in Fig. 3. One can see in Fig. 4b that the 2e′/2e″ bands are no longer degenerate at the **A** point for the distorted structure; a 0.75 eV band gap is introduced. With the reduced symmetry induced by the breathing motion in **9**, the 2e′ and 2e″ bands mix together; a strongly avoided crossing occurs. The 2e′ band is stabilized

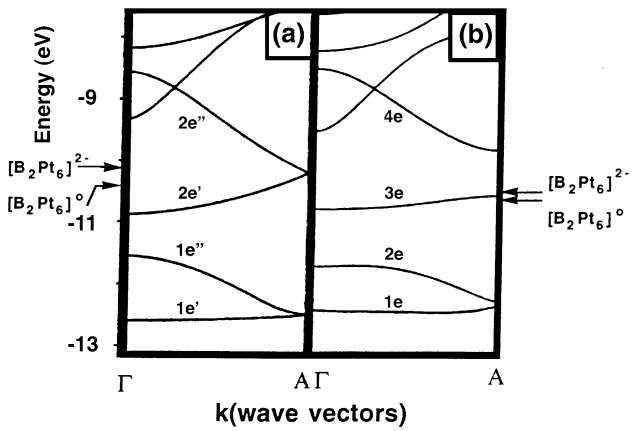

Fig. 4 Band structure for the prototype (**a**) and distorted (**b**) B_2Pt_6 chain; the position of the Fermi levels for $[B_2Pt_6]$ and $[B_2Pt_6]^{2-}$ is indicated by the *arrows*

at the **A** point, whereas 2e″ the band is destabilized. This is diagramed in **13** and **14**. An important portion of the

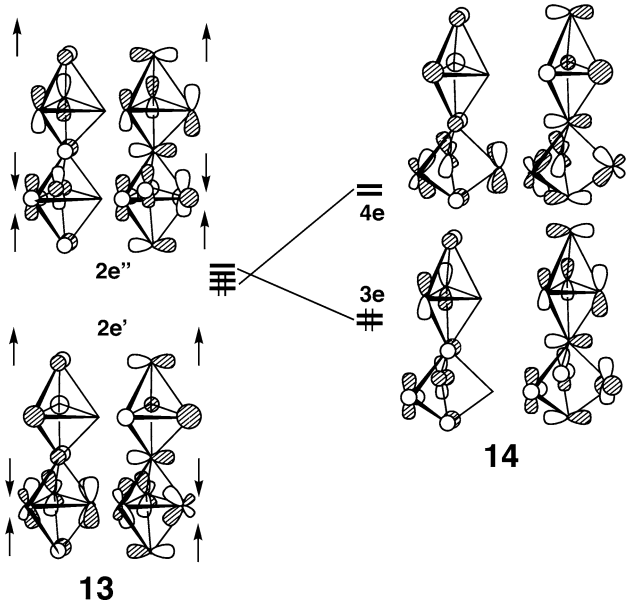

energetic driving force occurs in the B–B π bonding region. On going to the distorted structure, the 2e″ crystal orbitals gain π bonding in the squashed trigonal bipyramids (where the B–B distance has become short) and lose π antibonding in the elongated trigonal bipyramids. Exactly the opposite occurs to the 2e′ set in **13** upon distortion to 4e in **14**. Therefore, for $[B_2Pt_6]^{2-}$ with 68 electrons, the Fermi level is lowered from −10.17 to −10.52 eV along the distortion coordinate. This is a classic example of a Peierls instability at work. The distortion is highly favored for a 68 electron count that roughly corresponds to the electronic situation in $Ba_{2/3}Pt_3B_2$. But for chains with <66 electrons, the prototype structure will be favored. This is due to the destabilization of lower-lying bands. As mentioned in the fragment orbital analysis of a Pt_3B_2 trigonal bipyramid, boron p_x, p_y orbitals are predominant along with Pt s and p_x, p_y at the Fermi level. Notice that in both structures that the Pt and B e′ orbitals, analogous to the 1e′, 2e′, and 3e′ fragment orbitals in Fig. 3 are dominate around the Fermi level for $[B_2Pt_6]^{2-}$.

4 The three-dimensional structure

We are now in a position to study the electronic details for the full structure in the $M_xT_3B_2$ system. We first start our discussion with $Ba_{2/3}Pt_3B_2$. The alkali metal atoms are expected to provide an electrostatic potential only and thus have been deleted from the calculation. The Pt–Pt bond lengths within each trigonal bipyramid have been chosen to be 3.09 Å, an averaged value of 2.85 and 3.30 Å in the

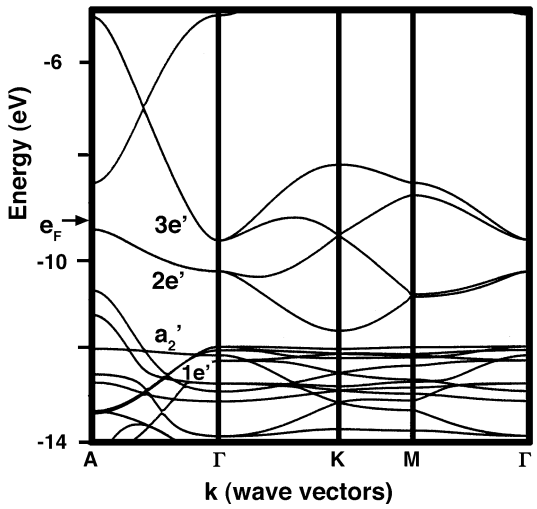

Fig. 5 The energy versus k plot for $Pt_3B_2^{4/3-}$ with the prototype structure where the Fermi level is indicated by e_F

experimental structure. It should be noted that the Pt–Pt distance between the trigonal bipyramids was 2.65 Å as it is in the experimental structure. Therefore, we expect there to be considerable Pt–Pt overlap along the **c**-axis (see Fig. 2). The Pt–B distances are 2.22 Å and B–B distances (again averaged) are 2.65 Å. The band structure is given in Fig. 5. The Fermi level for $Pt_3B_2^{4/3-}$, given by the arrow crosses several bands; this material expected to be a metal, which is accord with experiment [20]. On the band structure diagram of Fig. 5, four bands have been labeled according to the D_{3h} symmetry at the **Γ** point. The energy range between about −11 and −15 eV corresponds to the 15 platinum d bands. This includes 1e′ which can be identified with the molecular orbital 1e′ in Fig. 3 and a_2' which corresponds to molecular a_2' in **6**. Because of the long equatorial distances between platinum atoms, most of the occupied bands show only a gentle dispersion along the crystallographic **a** and **b** directions. The energy levels of Pt lie in the region of the energy band where the B–B interactions are bonding ones. This is due to the fact that the energy of the metal d atomic orbitals lie between the boron valence 2s and 2p orbitals. This also has been noted in the TB_2 (T = Sc, Ti, V, Cr, Mn) system [66]. The greatest dispersion of the platinum-centered bands run along the **Γ**–**A** direction. The crystal orbitals that are important to our discussion are labeled 2e′ and 3e′. The 2e′ and 3e′ sets are primarily Pt s and p in character mixed in a σ bonding way to boron p. There is also considerable Pt–Pt σ overlap between the trigonal bipyramids in these crystal orbitals. At **Γ**, their energy is lower than that in a discrete trigonal bipyramid because of inter-unitcell bonding interactions. At the **Γ** point, the 2e′ band orbitals are comprised of the 2e′ HOMO for a discrete trigonal bipyramid (**4** and **5**) in Fig. 4. This is shown in **15**. The 3e′ bands lie at

higher energy along the **Γ** to **A** line because they consist primarily of Pt *s* and *p* character. Furthermore, they are only weakly Pt–Pt intercell bonding. Both 2e′ and 3e′ orbitals possess e″ symmetry at the **A** point. The 2e″ crystal orbitals, shown in **16**, matchup with the molecular e″ set, **7** and **8**. This band does rise up much energy because it is still strongly Pt–Pt σ bonding at **A**. On the other hand, the 3e′ to 3e″ band is considerably destabilized along the **Γ** to **A** because at **A** the crystal orbital consists

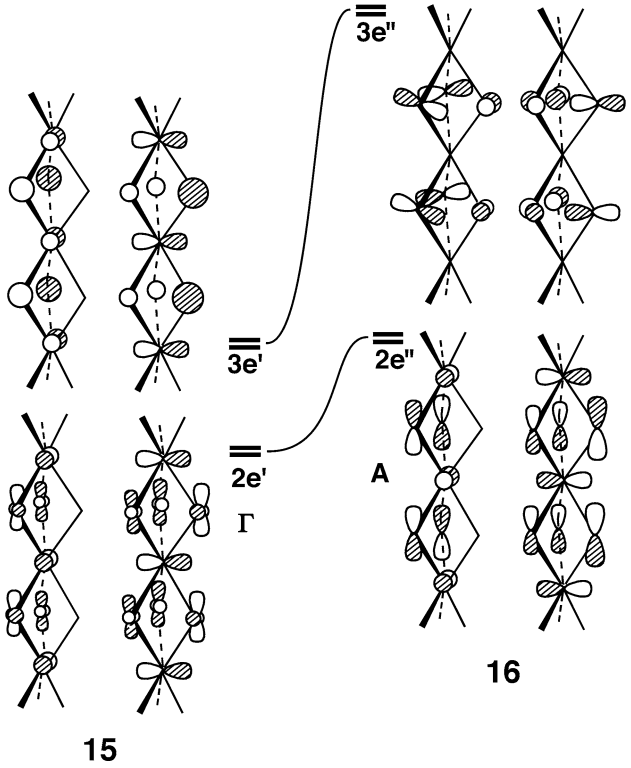

exclusively of Pt *p* character and is intercell Pt–Pt non-bonding. The density of states (DOS) plot of this structure is shown in Fig. 6 for the energy regions around the Fermi level, e_F.

The dashed line indicates the projection of B character and the dotted line is the projection of Pt *s* and *p* AOs. As indicated by Fig. 5 and **15**, there is considerable Pt *s*, *p* and B character just below the Fermi level. The consequence of this has also been seen in the molecular and one-dimensional models, namely electron density from boron is donated to platinum and this partially fills the Pt *s* and *p* states. In other words, the formal oxidation state of Pt is negative. This is then a situation where the energy of 5*d* AOs on platinum can be raised relative to the 6 s AO in a calculation, which includes electron–electron interaction and relativistic corrections [67]. It is this filling of platinum *s* and *p* that reinforces Pt–Pt bonding along the **c**-axis. Furthermore, it is the electron deficiency at boron that allows the formation of B–B σ and π bonding again along the **c**-axis.

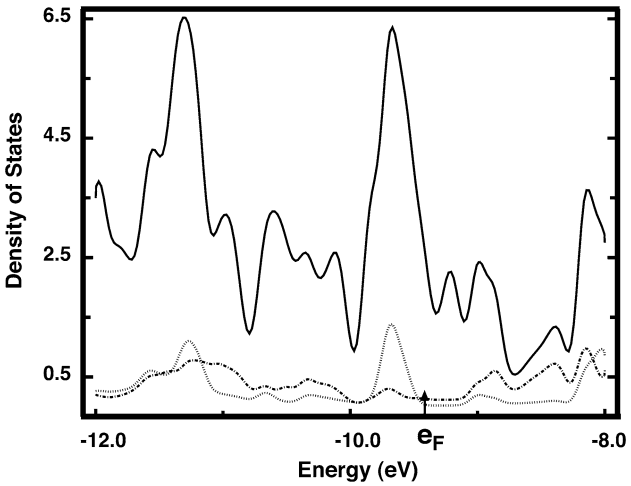

Fig. 6 The density of states versus energy plot for the prototype $Pt_3B_2^{2/3-}$ structure where the *dotted line* indicates the projection of Pt *s* and *p* orbitals, the *dashed line* is the projection of B AOs and the position of the Fermi level is given by e_F

We have doubled the unitcell for the investigation of the electronic structure for $Ba_{2/3}Pt_3B_2$ at the experimental structure. Recall that the platinum triangles stretch and contract in the **ab** plane (see **1** and Fig. 2). Figure 7 shows band structure along **Γ** to **A** with the 1e′–3e′ bands folded as the unitcell is doubled. Figure 7a corresponds to the prototype structure for the selected bands in Fig. 5, which have been labeled e′ for the symmetric and e″ for the antisymmetric combination of the unit cells. The corresponding bands from **Γ** to **A** at the experimental structure

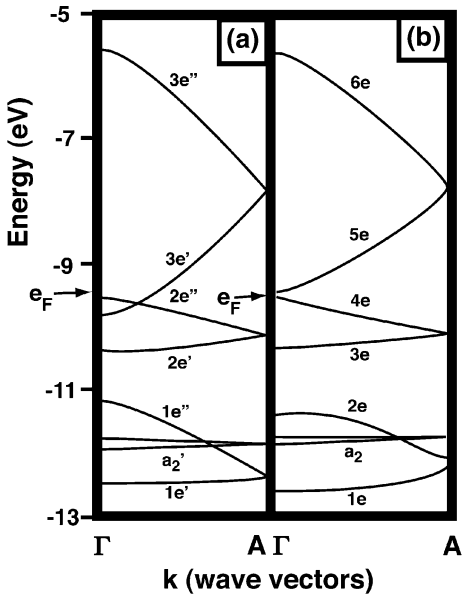

Fig. 7 The state energy versus k plot on going from **Γ** to **A** for the prototype (**a**) and experimental (**b**) structures where the position of the Fermi level is given as e_F

are shown in Fig. 7b. Upon distortion, several bands mix with each other just like in the one-dimensional model. In particular, the 3e′ band mixes into 1e″, which causes the former to be pushed up in energy around **Γ** to give 5e. The latter, 1e″, is stabilized around the **Γ** point to give 2e. The mechanism is analogous to that illustrated in **13** and **14** and will not be repeated here. The a_2', 2e′, and 2e″ do not change much in energy, nor does the position of the Fermi level. Around the **A** point, the 2e and 1e bands are destabilized at the experimental structure compared to 1e′ and 1e″, respectively, at the prototype due to the development of metal–boron σ^* interactions. Which geometry is favored is then a delicate situation that depends upon electron count. With a 74.67 electron count and 2e″ (4e) fully occupied, the experimental structure is preferred by 0.25 eV for the three-dimensional $Pt_6B_4^{8/3}$. However, compounds with <72 electrons that have the 2e′ band occupied prefer the prototype structure. For example, with 66 electrons (analogous to $Os_6B_4^{6-}$), the prototype structure is favored by 1.25 eV. The rationale is the following: The a_2' band in Fig. 7 is analogous to the HOMO in a discrete $Os_3B_2^{3-}$ trigonal bipyramid molecule (see **6**). It is not dispersed along Γ–**A** line since it does not have significant overlap along **c** direction. The corresponding Fermi level for a 66 electron count is −11.40 eV. So the portion of the 1e″ (2e) band is around **A** is filled and, of course 1e′ (1e) is totally filled. Both circumstances favor the prototype structure. Thus, it is expected that the prototype structure will be more stable for systems with a 66 electron count.

The computed overlap populations of the B–B and Pt–Pt bonds for the prototype and experimental structures differ greatly. In the prototype, the B–B overlap population was 0.082. Upon distortion, this raises to 0.245 for the short B–B distances in the squashed trigonal bipyramids and is reduced to 0.027 for the elongated trigonal bipyramids. As a point of reference, the B–B overlap population in B_2H_6 is 0.309 with a B–B distance of 1.74 Å. The Pt–Pt overlap population along the **c**-axis was computed to be 0.183 in the prototype and 0.177 for the experimental structure. For reference, the Pt–Pt overlap population in $Pt_2(CNH)_6^{2+}$ was computed to be 0.335. In this compound, there is an undisputable Pt–Pt single bond. The Pt–Pt overlap populations in the **ab** plane were found to be 0.002 for the prototype and 0.044 and −0.019 for the elongated and squashed trigonal bipyramids, respectively, in the experimental structure. In other words, metal–metal bonding is strong along the **c**-axis but negligible in the **ab** plane.

We have analyzed the electronic structure of $Os_3B_2^{3-}$ as a representative of a $CeCo_3B_2$ type compound. The dispersion of the energy bands calculated for the $Os_3B_2^{3-}$ lattice along the high symmetry lines of the hexagonal brillouin zone is similar to that shown in Fig. 5. The major difference is that the Os–Os distances in the **ab** plane are now much shorter as mentioned in the Introduction. Consequently, there is much more dispersion on going from **Γ** to **K** to **M**. The $Os_3B_2^{3-}$ trigonal bipyramid has five less electrons than $Pt_3B_2^{2-}$; hence, the a_2' orbital will be the highest occupied band, which is a partially occupied Os–Os σ^* d_{xy}, $d_{x^2-y^2}$ combination. This band is also the most dispersive among the *d*-block bands. As discussed earlier, it is constructed from the a_2' molecular orbital, **6**. All the inter-ring Os–Os contacts have an antibonding interaction as shown in **17** at the **Γ** point and the band lies at high energy. The a_2' units are partially in-phase with respect to each other, and consequently, the band is stabilized at the **K** point. At the **M** point, the a_2' unitcell orbitals alternate in their phases along the crystallographic y direction. The resulting inter-ring Os–Os contacts have σ bonding along the y direction and are nonbonding along the x direction, so that the bond orbital is

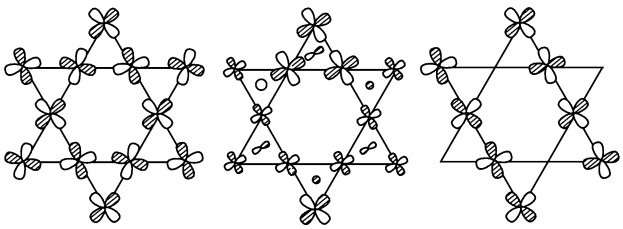

17

stabilized. The total density of states calculated for the *d* block bands and projection of the d_{xy}, $d_{x^2-y^2}$ orbital are shown in Fig. 8. The Os *d* orbitals are concentrated below −9.9 eV and B *p* orbitals are predominantly above −9.9 eV. The Fermi level is at −10.24 eV in an energy region where boron character is nearly negligible. There are large contributions of Os d_{xy}, $d_{x^2-y^2}$ orbitals at the Fermi level. The dashed line in Fig. 8 indicates the

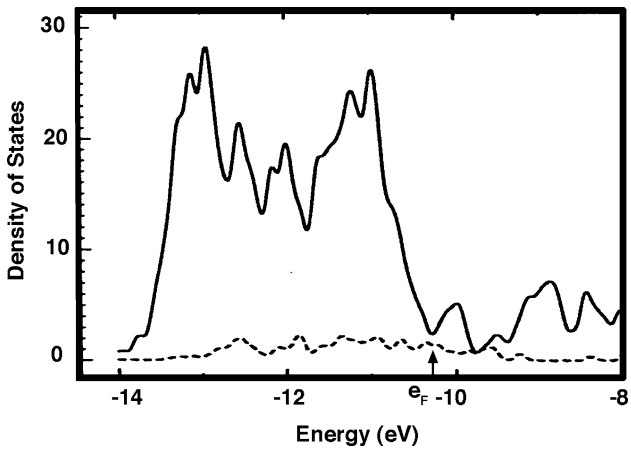

Fig. 8 The density of states versus energy plot for $Os_3B_2^{3-}$ where the projection of Os d_{xy} along with $d_{x^2-y^2}$ is given by the *dashed line* and the Fermi level is marked e_F

projection of these orbitals. Compared to $Pt_3B_2^{2/3}$, there is not much mixing of Os *p* into the occupied states. Furthermore, the dominance of metal *d* contributions in the **ac** plane has structural implications that we have referred to before. Namely, there is weak Os–Os bonding along the **c**-axis and strong bonding in the **ac** plane. The computed overlap populations reflect this with 0.059 for vertical and 0.121 for equatorial bonds.

Our calculations in this paper are semi-quantitative at best. It is certainly a difficult (and risky) matter to predict the structure of solid-state materials. But what we have demonstrated is that compounds with a low electron count should have a $CeCo_3B_2$ type of structure, whereas those with a larger electron count should possess a structure akin to $Ba_{2/3}Pt_3B_2$. To asses this on a more quantitative scale, we carried out calculations on $T_6B_4^q$ at both geometries using Pt parameters for the T atom at different charges, q. The resulting energy differences are graphically displayed in Fig. 9. The result is encouraging in that it correctly predicts compounds with electron counts of 33–34.5 electrons per formula unit should have the $CeCo_3B_2$ type of structure, while those with more than 36 electrons per formula unit should adopt a $Ba_{2/3}Pt_3B_2$ type of structure. But this is not the whole story since $CeCo_3B_2$ itself possesses 72 electrons in the doubled unit cell and clearly from Fig. 9 it should be distorted. But to be fair, there are several $M_xRh_3B_2$ compounds at the same electron count that do have the $Ba_{2/3}Pt_3B_2$ structure [15]. Perhaps, the energy differences in Fig. 9 are exaggerated somewhat and not only electronic effects but also the size of the alkaline and rare earth cations play a role in setting the structure. We also hasten to add that there are many other alternatives to these two structural types [28]; this is an area with a rich and complicated diversity.

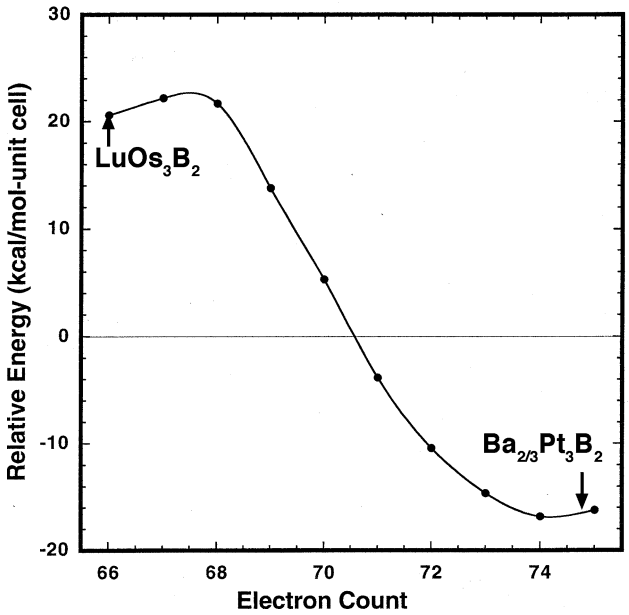

Fig. 9 The calculated energy difference between the $CeCo_3B_2$ and $Ba_{2/3}Pt_3B_2$ type of structure for $Pt_6B_4^q$ where q is the charge on the compound

5 Conclusions

The electronic structures of $Ba_{2/3}Pt_3B_2$ and $LuOs_3B_2$ have been analyzed by means of a molecular Pt_3B_2 fragment and one-dimensional analogs. Particular attention has been given to those bands at the Fermi level in both compounds. Our calculations on $Ba_{2/3}Pt_3B_2$ show that the states around the Fermi level primarily consist of Pt *s* and *p* character. There is electron transfer from boron to platinum, so that there should be a negative oxidation state associated with the Pt atoms. This electron transfer in turn allows the formation of B–B dimers and significant Pt–Pt bonding along the **c**-axis along with an attendant distortion of the Kagome net of metal atoms. With fewer electrons, as in $LuOs_3B_2$, this distortion is not expected to occur and instead there is strong metal–metal bonding in the **ab** plane. The Fermi levels for these compounds are dominated by Os *d* orbitals in the **ab** plane that are antibonding with respect to each other.

Acknowledgments We wish to thank the Robert A. Welch Foundation and the Texas Center for Superconducivity at the University of Houston for support of this work.

References

1. Nesper R (1991) Angew Chem Int Ed 30:788
2. Cotton FA (1966) Q Rev Chem Soc 20:389
3. Cotton FA, Murillo CA, Walton RA (2005) Multiple bonds between metal atoms, 3rd edn. Springer, New York
4. Mingos DMP, Wales DJ (1990) Introduction to cluster chemistry. Prentice Hall, Englewood Cliffs
5. Matthias BT, Corenzwit E, Vandenberg JM, Barz H (1977) Proc Natl Acad Sci USA 74:1334
6. Vandenberg JM, Matthias BT (1977) Proc Natl Acad Sci USA 74:1336
7. Shenoy GK, Dunlap BD, Fradin FY (1981) Ternary superconductors. Elsevier, New York
8. Kuz'ma YuB, Krip'yakevich PI, Biloninhko NS (1969) Dopovidi Akad Nauk USSR A10:939
9. Niihara K, Yashima S (1973) Bull Chem Soc Jpn 46:770
10. Rogl P (1973) Monatsh Chem 104:1623
11. Rogl P (1975) Monatsh Chem 106:1624
12. Valovka IP, Kuz'ma YuB (1978) Inorg Mater 14:356
13. Johnston DC (1977) Solid State Commun 24:699
14. Ku HC, Meisner GP, Acker F, Johnston DC (1980) Solid State Commun 35:91
15. Ku HC, Meisner GP (1981) J Less-Common Met 78:99
16. Vandenberg JM, Barz H (1980) Mater Res Bull 15:1493
17. Barz H (1980) Mater Res Bull 15:1489
18. Voroshilov YuV, Kripyakevich PI, Kuz'ma YuB (1971) Sov Phys Crystallogr 15:813

19. Rogl P (1980) J Nucl Mater 92:292
20. Shelton RN (1978) J Less-Common Met 62:191
21. Jung W, Quentmeier D (1984) Z Kristallogr 151:172
22. Wells AF (1977) Three-dimensional nets and polyhedra. Wiley, New York
23. Hahn T (ed) (1983) International tables for crystallography, vol. A: space-group symmetry. Reidel Dordrecht, Netherlands
24. Laves F (1967) In: Westbrook JH (ed) Intermetallic compounds. Wiley, New York, p 129
25. Pearson WB (1972) The crystal chemistry and physics of metals and alloys. Wiley, New York
26. Johnston RL, Hoffmann R (1990) Polyhedron 9:1901
27. Johnston RL, Hoffmann R (1992) Z Anorgan Allgem Chem 616:105
28. Cenzual K, Chabot B, Parthe E (1988) Acta Cryst C44:221
29. Voroshilov YuV, Krypyakevich PI, Kuz'ma YuB (1971) Sov Phys Cryst 15:813
30. Jung W, Quentemier D (1980) Z Krist 151:172
31. Hiebl K, Rogl P, Uhl E, Sienko MJ (1980) Inorg Chem 19:3316
32. Chevalier B, Cole A, Lejay P, Etourneau J (1981) Mater Res Bull 16:1067
33. Vandenberg JM, Barz H (1980) ibid 15:1493
34. Umarji AM, Dhar SK, Malik SK, Vijayaraghavan R (1987) Phys Rev B 36:8929
35. Bailey MS, Lobkovsky EB, Hicks DG, Claus H, Hor YS, Schlueter JA, Mitchell JF (2007) J Solid State Chem 180:1333
36. Mirgel R, Jung WJ (1988) Less-Common Met 144:87
37. Takegahara K, Harima H, Kasuya T (1985) J Phys Soc Jpn 54:4743
38. Wade K (1976) Adv Inorg Chem Radiochem 9:446
39. Mingos DMP (1984) Acc Chem Res 17:311
40. Lauher JW (1978) J Am Chem Soc 100:5305
41. Jemmis ED, Jayasree EG (2003) Acc Chem Res 36:816
42. Jemmis ED, Balakrishnarajan MM, Pancharatna PD (2002) Chem Rev 102:93
43. King RB (1990) Inorg Chem 29:2164 has used a different electron counting scheme but also obtains the same number of valence electrons for the trigonal bipyramidal clusters. With 18 electrons, each edge then could be considered to be a localized two center—two electron bond
44. Dahr SK, Malik SK, Vijayaragavan R (1981) J Phys C: Solid State Phys 14:L321
45. Oesterreicher H, Parker FT, Misroch M (1977) Appl Phys 12:287
46. Whangbo M-H, Hoffmann R, Woodward RB (1979) Proc R Soc London Ser A 366:23
47. Hoffmann R (1963) J Chem Phys 39:1397
48. Hoffmann R, Lipscomb WN (1962) J Chem Phys 36:2179
49. Ammeter JH, Bürgi H-B, Thiebeault JC, Hoffmann R (1978) J Am Chem Soc 100:3686
50. Taylor NJ, Chieh PC, Carty AJ (1975) J Chem Soc, Chem Commun 448
51. Longoni G, Chini P (1976) J Am Chem Soc 98:7225
52. Cotton FA, Haas TE (1964) Inorg Chem 3:10
53. Wei CH, Dahl LF (1968) J Am Chem Soc 90:3960
54. Ruff JK (1971) ibid 93:2159
55. Lauher JW (1978) ibid 100:5305
56. Dedieu A, Hoffmann R (1978) ibid 100:2074
57. Schilling BER, Hoffmann R (1979) ibid 101:3456
58. Evans DG, Hughes GR, Mingos DMP, Bassett J-M, Welch AJ (1980) J Chem Soc Chem Commun 1255
59. Delley B, Manning MC, Ellis DE, Berkowitz J, Trogler WC (1982) Inorg Chem 21:2247
60. Rives AB, Xiao-Zeng Y, Fenske RF (1982) ibid 21:2286
61. Pacchioni G, Fantucci D, Valenti V (1982) Inorg Chem Acta 224:89
62. Fantucci P, Pacchioni G, Valenti V (1984) Inorg Chem 23:247
63. Chang KW, Wooley RG (1979) J Phys C: Solid State Phys 12:2745
64. Bullet DW (1985) Chem Phys Lett 115:450
65. Underwood DJ, Hoffmann R, Tatsumi K, Nakamura A, Yamamoto Y (1985) J Am Chem Soc 107:5968
66. Burdett JK, Canadell E, Miller GJ (1986) J Am Chem Soc 108:6561
67. Whangbo M-H, Lee C, Köhler J (2006) Angew Chem Int Ed 45:7545